

A Facile Route to ZnO Nanoparticle Superlattices: Synthesis, Functionalization, and Self-Assembly

Lan Chen,^{*,†} Ju Xu,[‡] Justin D. Holmes,^{†,‡,§} and Michael A. Morris^{*,†,‡,§}

Department of Chemistry, University College Cork, Cork, Ireland, Tyndall National Institute, Cork, Ireland, and Centre for Research on Adaptive Nanostructures and Nanodevices (CRANN), Trinity College Dublin, Dublin, Ireland

Received: September 4, 2009; Revised Manuscript Received: December 15, 2009

Highly ordered, free-standing, complex, two- or three-dimensional (2D or 3D) nanoparticle superlattice arrays were created by either evaporation-induced self-assembly or precipitation-induced self-assembly from the size-monodispersed ZnO nanoparticles functionalized by carboxylic and alkylthiol ligands. The synthesis of the constituent ZnO nanoparticles is both novel and facile and is suggested as a generic means of producing oxide nanomaterials by reaction of metal cations and oxide anions in alcohol solutions at room temperature. The regularity of the nanoparticle products and their chemical functionalization provides the means to achieve superlattice thin films on indium tin oxide (ITO)-coated glass slides. Low-angle XRD, SEM, and TEM confirm the formation of these highly organized, 2D or 3D self-assembled superlattices that adopt an unusual primitive cubic structure. The properties of the nanoparticles and the superlattices are also described in the paper.

1. Introduction

Structural regularity (size and shape monodispersivity) in nanoparticle synthesis was first demonstrated for silica using the Stöber method,¹ and this has resulted in the development of a number of advanced particle technologies and creation of regular nanoparticle arrangements (artificial opals) for application in photonics. There would be a number of applications possible if the regular arrangements seen in silica nanoparticle structures could be extended to more functional materials. However, extension of the silica synthesis methodology to other oxide materials has been frustratingly difficult. Nanoparticulate ZnO is perhaps an ideal choice, having a number of important properties and applications,^{2–7} and the development of novel nanoparticle synthesis methods that can exert both dimensional and stoichiometric control is of pivotal importance because of the relationship of structure to property at small sizes.^{3,7–13} Extending established methods to allow (crystal) structure and composition within the nanoparticle (NP) to be defined while providing precise shape and size control for particle superlattice formation is the goal of the work reported here.

One of the barriers to the development of these methods is the indirect nature of the synthesis methods necessitating formation of intermediate compounds (carbonates, hydroxides, alkoxides, etc.) via precipitation, evaporation or hydrolysis, and subsequent dehydration/thermal decomposition processing that can result in particle agglomeration with deleterious results.^{10,12,14–19} The direct (i.e., via reaction with solution-phase oxygen anions) synthesis of ZnO from Zn²⁺ in solution is generally considered impossible because oxygen anions in solution are thought not to form. The oxidation of organometallic zinc in solution or metallic zinc in oxygen can form ZnO directly, but either the oxidation is incomplete or the stoichiometric control is difficult in these cases.^{8,20,21} Moreover, organometallic precursors are

usually expensive and/or air- or moisture-sensitive, which can make synthesis and processing difficult. Herein, we develop a novel and facile route to synthesize size-monodispersed ZnO NPs directly in anhydrous alcohol solutions at room temperature (RT). We show, for the first time, that this route can be tailored using surface “capping agents” to yield highly organized, two- or three-dimensional (2D or 3D) self-organized superlattices by either evaporation-induced self-assembly (EISA) or precipitation-induced self-assembly (PISA). For the first time, definitive proof (in contrast to local area TEM imaging) shows that large area oxide NP superlattices are regular enough and extend over significant areas to form well-defined X-ray diffraction patterns that can be used to classify the structure and to be imaged directly by SEM. The nanoparticle synthesis method is much simpler than previous reports, avoiding complex or multistep reaction schemes, organometallic preparations, and expensive equipment, and we believe it offers a new procedure for synthesis of many metal oxides that allows rapid preparation of regularly shaped materials of controlled stoichiometry.

2. Experimental Section

2.1. Materials. All chemicals are reagent grade and used as-received. Na₂O (97%), ZnCl₂ (99%), oleic acid (OLA), 1-dodecanethiol (98%, DT), 16-mercaptophexadecanoic acid (MPA), ITO-coated glass slides, methanol, and anhydrous ethanol are purchased from Aldrich. Alkylamines, for example, octylamine, 1-dodecylamine, and hexadecylamine, are purchased from Fluka.

2.2. Synthesis of Bare ZnO NPs. A 20 mL portion of 0.1 M Na₂O ethanol solution was slowly added in 20 mL of 0.1 M ZnCl₂ ethanol solution under vigorous magnetic stirring at room temperature (RT) for 3 h. The resulting cloudy solution, when the concentration is low, or the white precipitate, when the concentration is high, was filtered on a piece of filter paper (0.2 µm pore size) and washed with ethanol and then acetone twice. The wet product was dried at 60 °C overnight.

2.3. In Situ Synthesis/Functionalization of ZnO NPs. This synthesis procedure is the same as the above one except that 2 mmol of hexadecylamine and 1 mmol of oleic acid were added

* To whom correspondence should be addressed. E-mail: m.morris@ucc.ie (M.A.M.), lan.chen@ucc.ie (L.C.).

† University College Cork.

‡ Tyndall National Institute.

§ Trinity College Dublin.

in 20 mL of 0.1 M Na_2O and ZnCl_2 ethanol solution, respectively, prior to the mixing of two solutions. The mixture of two portions of solution was stirred at RT for 3 h. The precipitation of the oleic-acid-capped nanoparticles in alcohol solution is derived of the “energy minimization” caused by the interaction between the hydrophobic shells and the polar solvent molecules where the outward alkyl (oleyl) moieties on the capped nanoparticle are more hydrophobic than those of free oleic acid molecules due to the “screen” of the inward hydrophilic (carboxylic) heads by the outer hydrophobic (tail) shell on the capped NPs. Indeed, the solution changes turbidity, followed by the immediate (in a few seconds) formation of white precipitate as soon as two portions of “clear” (a little cloudy at RT but clearer at the elevated temperature, e.g., 60 °C) reactant solutions are mixed together where the PISA is achieved during the formation of the precipitate. To get size-monodispersed nanoparticles, the as-formed precipitate with the solution together was aged at 60 °C overnight. The product was collected by filtration on a piece of filter paper. The wet product was completely dispersed in 20 mL of toluene to remove the uncapped ligand (oleic acid or hexadecylamine) residues into which 80 mL of methanol was poured, and a white precipitate was formed immediately. The product was collected by filtration again, and the wet precipitate was dried at 60 °C overnight to get the OLA–ZnO NPs.

2.4. Ex Situ Functionalization of ZnO NPs. The ex situ functionalization happens as an exchange reaction between the capping ligand bound on the NP surfaces and the free capping ligand in the solution. Two portions of OLA–ZnO nanoparticle samples (1 mmol based on Zn element) were dissolved in 10 mL of toluene, respectively. To one portion of 10 mL of OLA–ZnO toluene solution, 1.5 mmol (excess) of 1-dodecanethiol was added, and the mixture was stirred at RT for 2 h. An 80 mL portion of methanol was then added in the mixture to allow the formation of the white precipitate. The product, DT–ZnO, was collected by filtration and washed with ethanol and then acetone twice. The final DT–ZnO product was received after 10 h of drying at 60 °C. To another portion of 10 mL of OLA–ZnO toluene solution, 20 mL of 16-mercaptohexadecanoic acid methanol solution was slowly added under stirring at RT for 2 h. Thereafter, 80 mL of toluene was added in the mixture to obtain a white precipitate. The MPA–ZnO precipitate was collected by filtration and washed with toluene and then acetone twice. The final wet MPA–ZnO sample was dried at 60 °C for 10 h.

2.5. Self-Assembly of ZnO Nanoparticle Superlattice. A ZnO nanoparticle superlattice was obtained by evaporation-induced self-assembly (EISA) or precipitation-induced self-assembly (PISA). A given amount of OLA–ZnO was completely dissolved in 10 mL of hexane to form a homogeneous solution. The solution was evaporated spontaneously on either TEM grids or glass slides to form the 2D self-organized nanoparticle arrays in the former case and the transparent 3D nanoparticle superlattice thin film in the latter case. However, the formation of a 3D nanoparticle superlattice was also caused by PISA from a large quantity of OLA–ZnO NP (hexane) solution to which a quadruple volume of polar solvent, for example, methanol, was added.

2.6. Analyses. The powder samples were analyzed by a JEOL 2000FX transmission electron microscope (TEM) operating at 200 kV, a Phillips Xpert MPD X-ray diffractometer (XRD) using $\text{Cu K}\alpha$ radiation at a node voltage of 40 kV (with a high sensitivity X’Celerator detector), and a high performance AXIS 165 X-ray photoelectron spectrometer (XPS). The su-

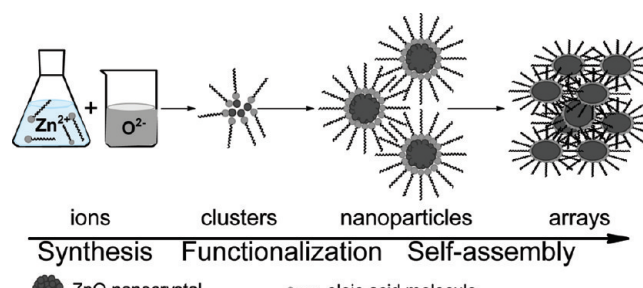


Figure 1. Schematic process for in situ synthesis, functionalization, and self-assembly of ZnO NP superlattices.

perlattice thin film analyses were carried out by a JEOL JSM 6700 scanning electron microscope (SEM) at 5 kV and a Cary 50 UV–vis spectrophotometer. In addition, UV–vis, photoluminescence, and FTIR spectra were recorded by a Cary 50 UV–visible spectrophotometer, a PerkinElmer LS50B fluorescence spectrometer, and a Bio-Rad FTS 3000 spectrometer, respectively.

3. Results and Discussion

The in situ process for generating uniform OLA–ZnO NPs proceeds in three different stages, illustrated schematically in Figure 1. Initially, unstable ZnO clusters are formed by reaction of Zn^{2+} and O^{2-} ions. In the second stage, many unstable ZnO clusters combine to form thermodynamically stable functionalized nanoparticles in the presence of capping ligand molecules. Alkylamines are added prior to the reaction and are not detected in the final product. They are considered as “spacers” that render the particles hydrophobic and partition the colloidal solution into well-defined nanoscale regions that inhibit particle growth and control dimensions. Finally, the oleic-acid-capped ZnO NPs (OLA–ZnO) self-assemble into an ordered superlattice array spontaneously out of solution. The synthesis reaction occurs by direct liquid-phase precipitation (DLPP) of ZnO from the mixing of Zn^{2+} ions and an equivalent amount of O^{2-} ions from a suitable source under anhydrous conditions at RT. Many anhydrous solvents can be used, but ethanol proved to be the most effective here. Anaerobic or aerobic conditions can both be used with no observable effect on product, confirming that the products are not formed by air oxidation. Further, reaction did not occur and no product was observed in the absence of an anion source, which, in our case, was either Li_2O or Na_2O . The reaction mechanism can be thought of as simply $\text{Zn}^{2+}(\text{sol}) + \text{O}^{2-}(\text{sol}) \rightarrow \text{ZnO} \downarrow$, but it is clear this is either a series of equilibria or a metathesis-type reaction. Work is underway to explore this mechanism.

3.1. Facile Syntheses of ZnO NPs. Uncapped bare NPs can be obtained from mixing an ethanol solution containing Zn^{2+} ions with a similar solution of alkali metal oxides at a molar ratio of 1 to 1, forming a white precipitate instantaneously. The X-ray diffraction (XRD) pattern shows the formation of well-crystallized and stoichiometric ZnO materials with a hexagonal (wurtzite) structure shown in Figure 2. The crystallite size is calculated at around 7 nm from the peak widths based on the Scherrer’s equation. The results show that the increase in the aging temperature in a low range (<100 °C) can raise the crystallinity of the ZnO NPs but results in the deterioration of the crystal growth when the temperature is higher than 100 °C. This is probably derived from the partial dissolution of the ZnO NPs in a higher-temperature range. Bare ZnO NPs have more sharp diffraction peaks than those ligand-capped NPs, as shown

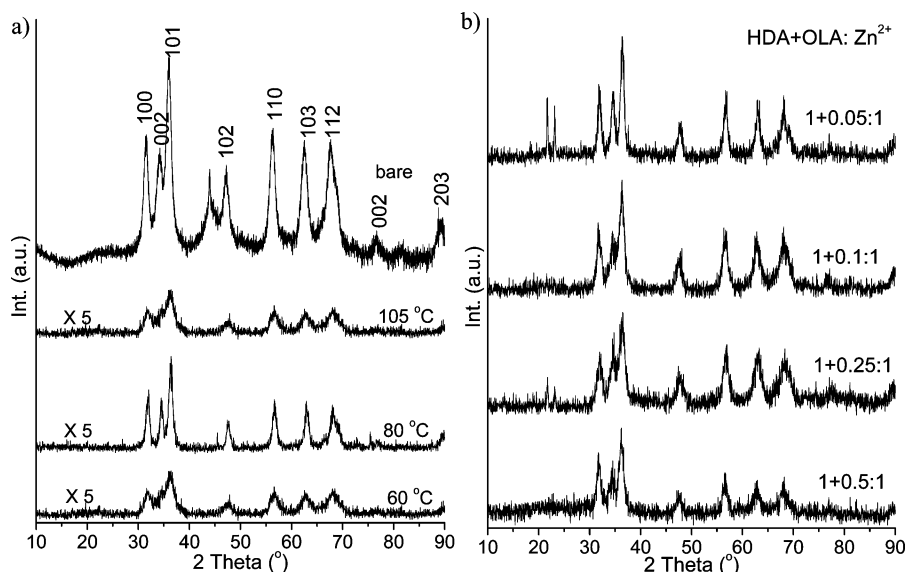


Figure 2. X-ray diffraction (XRD) patterns (JCPDS ref no. 36-1451). (a) Bare ZnO NPs and the oleic-acid-capped ZnO NPs aged in the mother solution under different temperatures and (b) OLA-ZnO synthesized with different oleic acid-to-Zn²⁺ ratios.

in Figure 2a. It is obvious that the long-chain ligand molecules can separate the primary ZnO NPs and inhibit the coarsening of those particles to form the smaller sized crystals (particles). The higher the ratio of the concentration of ligand to Zn²⁺ in the precursor solution, the smaller the obtained NPs are, as seen in Figure 2b.

The synthesis of the monodispersed ZnO NPs is achieved in the presence of both capping ligands terminated with strongly interacted carboxylic or thiol functional groups and spatially occupied “inert” alkylamine ligands. Transmission electron microscopy (TEM) images (Figure 3a–c) show the formation of size-monodispersed ZnO NPs with the identical size and shape for the NPs synthesized in the presence of alkylamine with the different carbon chain unit, for example, C₈, C₁₂, and C₁₆. In Figure 3a–c, the molar ratio of reactants—alkylamine/oleic acid/Zn²⁺—was kept at 1:0.5:1. The elemental composition of C, H, O, and N in the final products is analyzed by an elemental analyzer (model CE440) using high-precision thermal conductivity measured in the gaseous form of these elements. In all cases, elemental analysis provided an evidence of only trace nitrogen-containing materials in the final oxide nanoparticle products, confirming that the alkylamine probably acts only as a growth inhibitor, where the alkylamines actually exist in the as-formed particle precipitate and can be easily removed by the redispersion–reprecipitation cycles by toluene and then ethanol (twice). It is suggested that only oleic acid is chemically bound to the NP surface, while the alkylamine species act as a cocapping ligand to balance the carboxylic (oleic acid) effect during the synthesis and are not strongly absorbed on the particle surfaces since the particles grow larger without alkylamines than with them under the same conditions. These functionalized NPs are, therefore, labeled as OLA–ZnO NPs. There is almost no change in particle size with increasing carbon unit size—octylamine (OA) = 4.3 nm, 1-dodecylamine (DDA) = 4.4 nm, and hexadecylamine (HDA) = 4.4 nm. Figure 3d–f shows the particle sizes of 7.8, 6.4, and 6.9 nm, respectively, and it decreases with the decrease of the oleic acid content (see the Supporting Information, Figure S1a–f). The size difference between Figure 3a–c and Figure 3d–f comes from several aspects: (1) different Zn²⁺ concentrations; (2) different ratios of alkylamine to oleic acid, and (3) different synthesis temperatures (RT) in two separated batches. The room temperature

(no air conditioner) for the former batch (in winter) is about 5–9 °C lower than the latter one (in summer). For a given amount of HDA, the higher the OLA content, the stronger the acid–base interact between them and the lower the effective capping ligand concentration is since the HDA is a weak base, whereas the OLA is a weak acid. A higher OLA content results in the formation of the larger NPs, as seen in Figure 3d. However, the acid–base interaction can be negligible when the OLA concentration is so low compared with that of the HDA. The interaction between the OLA molecules and the ZnO NP is more significant than that between the OLA and HDA molecules under low-concentration conditions, so Figure 3f shows a bit increase in the particle size but broadened particle distribution profiles in comparison with Figure 3e due to the decrease in the ratio of OLA to Zn²⁺.

UV-vis spectra (Figure 4) show an obvious blue shift of the maximum absorbance wavelength related to the small size of the ZnO NPs, thought to be caused by the quantum size effect, as reported previously.²² The measured band-gap values are 3.24 and 3.59 eV for aggregated bulklike materials and well-dispersed nanoparticles, respectively. However, the surface-capped NPs have a lower absorbance intensity (peak) and a longer absorbance wavelength, which may be attributed to the quenching of the oxygen vacancies on the external surfaces of the ZnO NPs by the carboxylic group in the OLA molecules. The quenching by oleic acid on the vacancies (defects) on the external surface of a ZnO NP is considered to relax the dimension contraction (caused by increased proportion of surface atoms with the decreased dimensions) to some extent and, therefore, is equal to an increase of the particle size. The absorbance wavelength shifts to the red end of the visible-light spectrum from 346 to 351 nm. However, the lower absorbance intensity for the OLA–ZnO NPs may be ascribed as the screen effect of the capping ligand shell around the particles where quite a number of absorbable photons cannot be effectively captured by the ZnO core. It seems that the existence of the capping ligand cannot decrease the particle size but improves the particle dispersion, so the primary particle size should be formed during the precipitation rather than the dispersion process.

3.2. Functionalization of ZnO NPs. Surface functionalization of the ZnO NPs occurs either *in situ* in the presence of the

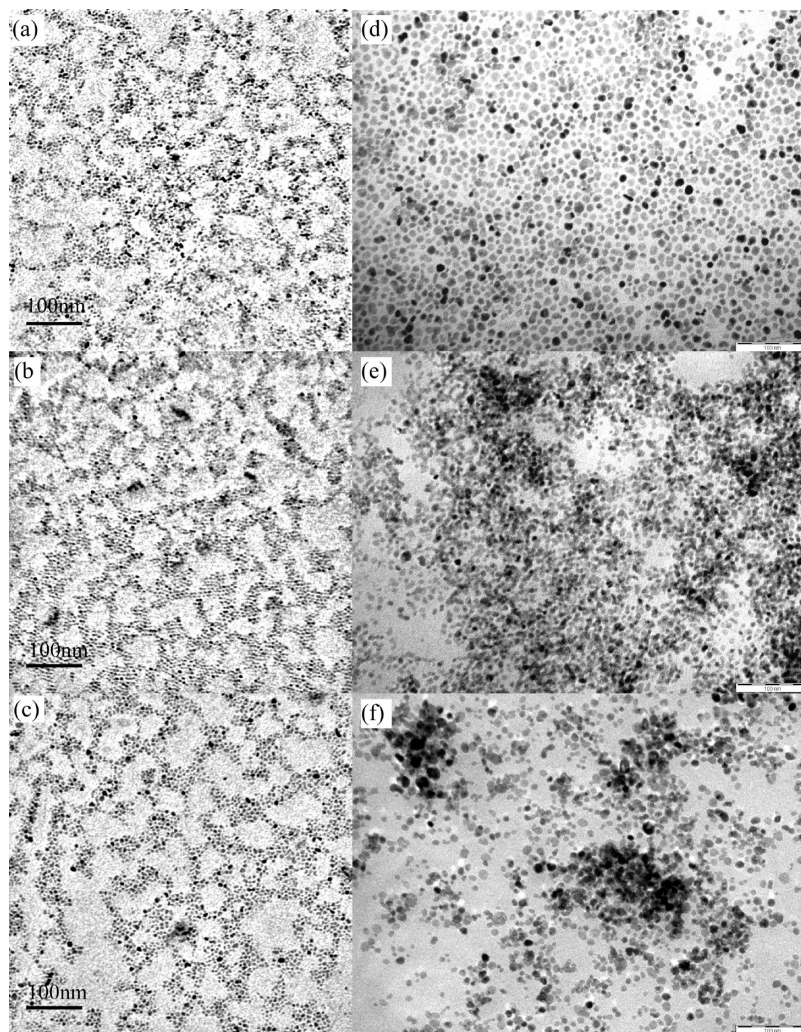


Figure 3. Transmission electron microscope (TEM) images of OLA-ZnO NPs obtained in the presence of (a) OA + OLA/Zn²⁺ (1 + 0.5:1), (b) DDA + OLA/Zn²⁺ (1 + 0.5:1), and (c) HDA + OLA/Zn²⁺ (1 + 0.5:1) in the Zn²⁺ concentration of 0.05 mM and HDA + OLA/Zn²⁺ (1 + 0.5:1), (1 + 0.1:1), and (1 + 0.05:1) for (d), (e), and (f) in the Zn²⁺ concentration of 0.04 mM. All scale bars are 100 nm.

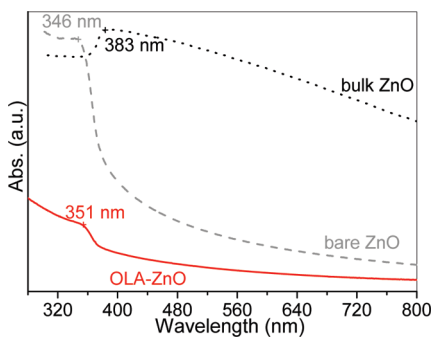


Figure 4. UV-vis absorbance spectra of ZnO colloidal solutions (bulk ZnO, bare ZnO NPs in ethanol, and OLA-ZnO NPs in hexane).

oleic acid and alkylamines in the synthesis or ex situ using strongly bound ligands to exchange the weaker ones after the synthesis of ZnO NPs. The exchange ability among different ligands decreases in an order of alkylthiols, carboxylic acids, alkylamines, and alcohols (for bare ZnO NPs). For instance, alkylamine-capped NPs can be stably formed after the addition of alkylamine in an alcohol–metal salt reaction system. Furthermore, oleic-acid-covered ZnO NPs are easy to be produced when the alkylamine-capped NPs meet oleic acid molecules in toluene. OLA-ZnO NPs have excellent solubility in nonpolar solvents due to the stable and complete coverage

of the long alkyl tail on the external surfaces of the nanoparticles. Oleic acid is bound to the nanoparticle surface via the terminal carboxylic groups presenting an alkyl exterior (as shown in Figure 5a). This is witnessed by a strong C–H absorbance peak at 1390 cm⁻¹ seen in the FTIR spectroscopy data for the capped particles shown in Figure 5b. Further evidence for selective binding of oleic acid is also provided by the FTIR data where there are peaks at 1557 and 2930 cm⁻¹, indicating C=O and CH₂ signals typical of carboxylic groups in the oleic-acid-capped ZnO NPs.^{23–25} Further, no N–H features at 1605 and 3330 cm⁻¹ are observed, consistent with the nonbinding of the alkylamine.²⁶ The elemental analysis also suggests the formation of oleic-acid-functionalized ZnO nanoparticles with an empirical formula equivalent to (ZnO)_{8.5}(OLA)₁. This value is consistent with calculations based on a monolayer of oleic acid ligands at the surface of a 4.5 nm particle.

However, the FTIR spectra for the ZnO nanoparticle thin films grown on glass slides show different features. As shown in Figure 5c, strong peaks at 2850 and 2950 cm⁻¹ indicate that the exterior organic “shell” of such OLA–nanoparticle complexes consists exclusively of methyl (CH₃, alkyl) groups. Low-energy “rocking” or “twisting” vibration of C–H (CH₂) at 1390 cm⁻¹, as shown in Figure 5b, is “frozen” in the dense nanoparticle films, and only high-energy “stretching” or “scis-

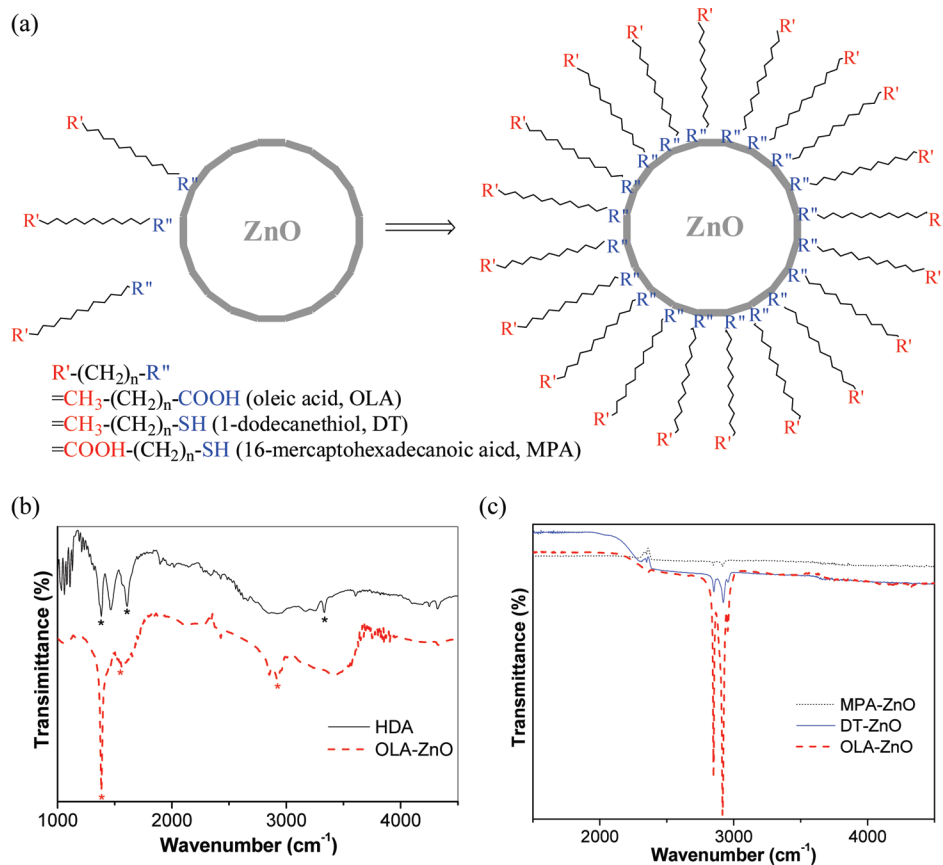


Figure 5. Functionalization of ZnO NPs. (a) A schematic process for the surface functionalization. (b, c) Fourier transform infrared spectroscopy (FTIR) of (b) hexadecylamine and free-standing oleic-acid-functionalized ZnO NPs and (c) ZnO NPs functionalized with different ligands grown on glass slides.

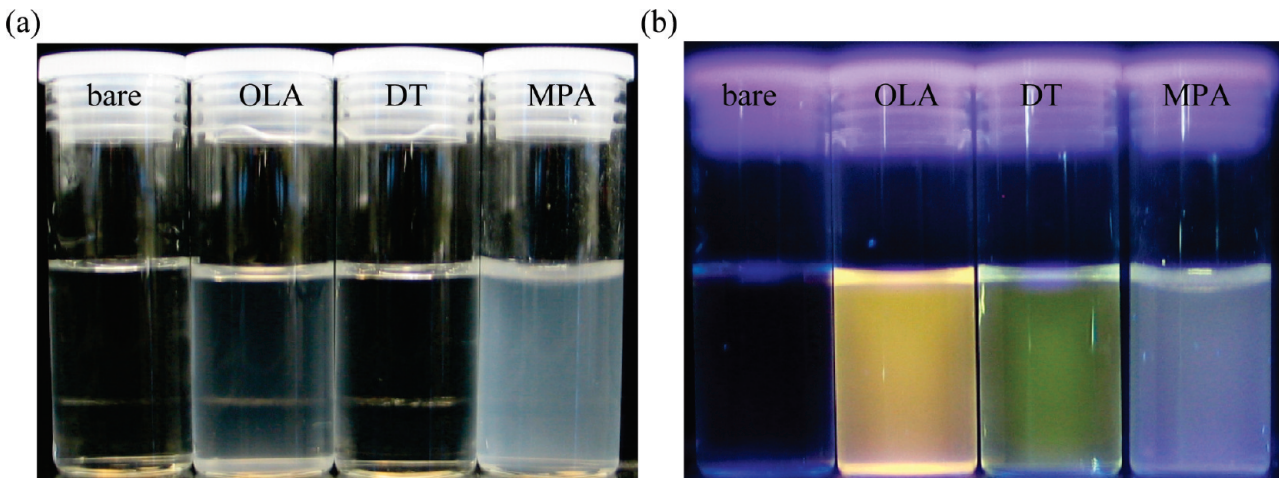


Figure 6. Photographs of ZnO NP solutions under (a) visible light and (b) ultraviolet light (365 nm). The bare, OLA-, DT-, and MPA-ZnO NPs are dispersed in water (for OLA- and MPA-ZnO) and hexane (for OLA- and DT-ZnO), shown from left to right.

soring" vibration of CH_2 at the range of 2850–2950 cm^{-1} is observed, as shown in Figure 5c.^{23–25,27}

Figure 6 shows that the solution color under the UV light is yellow, green, and cyan for the OLA-, DT-, and MPA-ZnO NP dispersions, respectively. The transmitted light color of the DT- and MPA-ZnO NPs shortened in the wavelength (blue shift) can be attributed to the partial sulfidation of the ZnO NP surfaces by the thiol groups of the DT and MPA molecules since the absorbance band gap of the ZnS NPs is wider than that of ZnO. Moreover, the sulfidation also makes the UV-vis absorbance peak shift to the blue end, as shown in Figure 7a. The whole absorbance band can be divided into 3 zones: the

near UV zone ("1", down to 250 nm), the UV zone ("2", 250–390 nm), and the visible zone ("3", 390–800 nm). Considering the absorbance blue shift caused by the size decrease,²² the absorptivity distribution with the absorbance wavelength can be used to explain the dispersivity distribution with the particle size. The relative absorbance intensity (compared to the total absorbance) of the bare ZnO NPs in the different zones decreases in the order of "3", "2", to "1", and the bigger absorbance intensity in zone 3 and smaller intensity in zone 1 show the quantity of the particle aggregates is more than that of the monodispersed NPs in the solution, which indicates its dispersivity is bad, as shown in Figure 7b. The

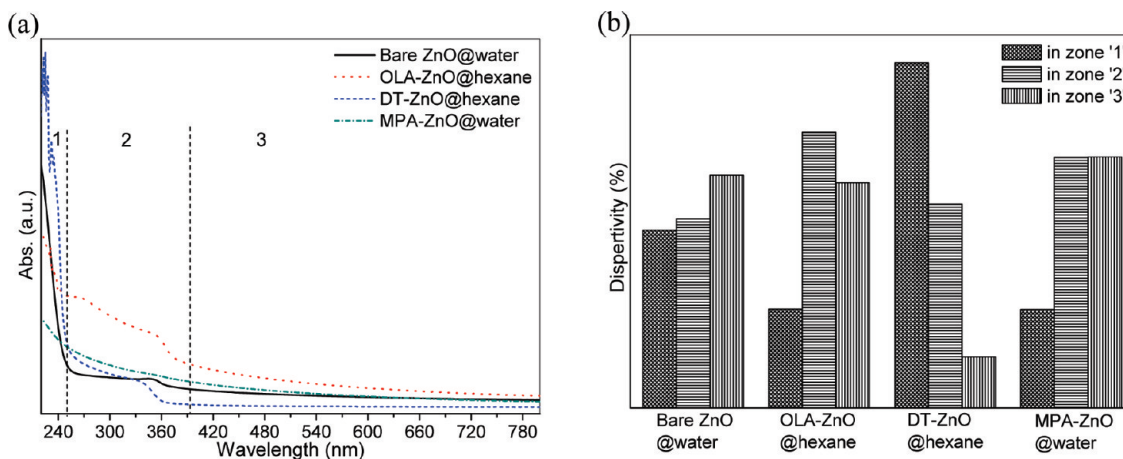


Figure 7. (a) UV–vis absorbance spectra of ZnO NPs functionalized with different ligands and (b) their dispersivity (%) determined by their corresponding absorptivity.

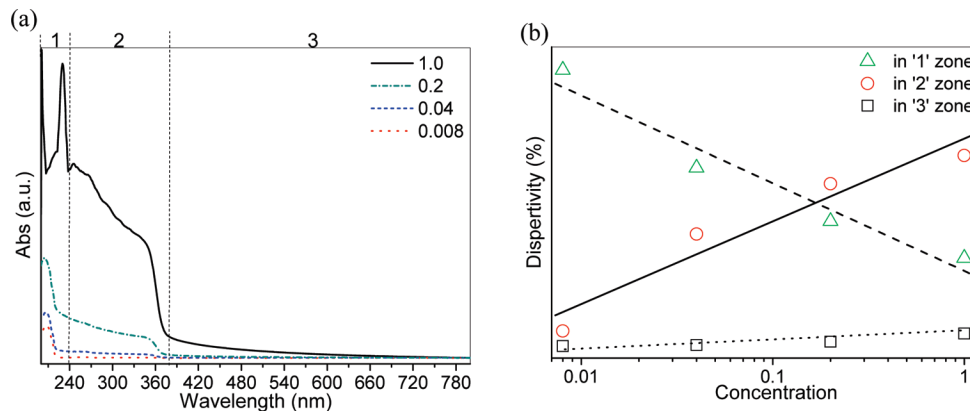


Figure 8. (a) UV–vis absorbance spectra of OLA–ZnO NPs in hexane with different (relative) concentrations and (b) the dispersivity (%) determined by the corresponding absorptivity.

total absorbance of the bare ZnO NPs is quite low compared with other functionalized NPs due to its low content in the solution. The DT–ZnO sample has the strongest absorbance in zone 1, showing that most NPs are monodispersed. As shown in Figure 6a, a clear DT–ZnO NP solution can be seen, confirming its excellent monodispersity. Both the OLA– and the MPA–ZnO NPs have a strong absorbance in zones 2 and 3 but smaller absorbance in zone 1, indicating a good dispersivity (total absorbance) but bad monodispersivity (near UV absorbance) due to the formation of particle aggregates where the colloidal turbidity can be seen in Figure 6a.

To check whether the aggregation results in the strong absorbance in zones 2 and 3, the original OLA–ZnO solution is diluted by the different volumes of hexane. It shows clearly that the diluted solution causes the decrease of the total absorbance over the whole wavelength (220–800 nm) and it decreases even more in zones 3 and 2 than that in zone 1, as shown in Figure 8a. The integrated absorbance intensity in zones 1 and 2 proportionates linearly to the particle concentration in solution, as shown in Figure 8b. The absorbance intensity in zone 1 increases linearly with the decrease of the NP concentration, while that in zone 2 decreases linearly, following the same pace with NP concentration in the solution. The absorbance increase in zone 1 shows the improvement of the NP monodispersivity, while the decrease in zone 2 means the dissolution of the NP aggregates. The slight change for the absorbance in zone 3 indicates the absence of the very big particle aggregates (up to $\sim 10^2$ nm) in the solution.

Photoluminescence spectra (Figure 9a) show the green emission peaks at 520–525 nm for all samples under an excitation wavelength of 350 nm. A smaller violet emission peak at the wavelength of 422 nm can be observed clearly in OLA–, DT–, and MPA–ZnO NPs where the change of its relative intensity to the green emission peak largely conforms to the color change in Figure 6b. The O 1s feature lines show different oxygen states on the NP surfaces for different ligands, as shown in the XPS spectra (Figure 9b). The bare ZnO NPs harvest the highest electron yield due to the complete exposure of their surfaces to the X-ray beam, while the functionalized surfaces give the decreased photoelectron yield due to the ligand-covered surfaces. The O 1s signal almost disappears in the DT–ZnO sample due to the complete substitution of the oxygen atom by the sulfur derived from the sulfidation of the thiol (SH) group of the DT molecules on the particle surface. Compared with OLA– and MPA–ZnO, the O 1s line of the bare ZnO NPs has the higher binding energy (531 eV) due to the formation of the OH⁻ species on their surfaces caused by the absorption of the H₂O molecules on the uncapped oxygen vacancies.^{28,29} OLA–ZnO NPs give a lower (529 eV) binding energy due to the elimination of the surface oxygen defects by the coverage of the –COOH group on their surfaces. However, the –COOH groups located in the exterior end of the MPA–ZnO NPs also yield the O 1s line at 530 eV, even though the ZnO surfaces are completely sulfidized by the –SH groups of the MPA molecules.

Finally, among all ligands used here, the most stably absorbed ligands on the surface of a ZnO nanoparticle are alkylthiols,

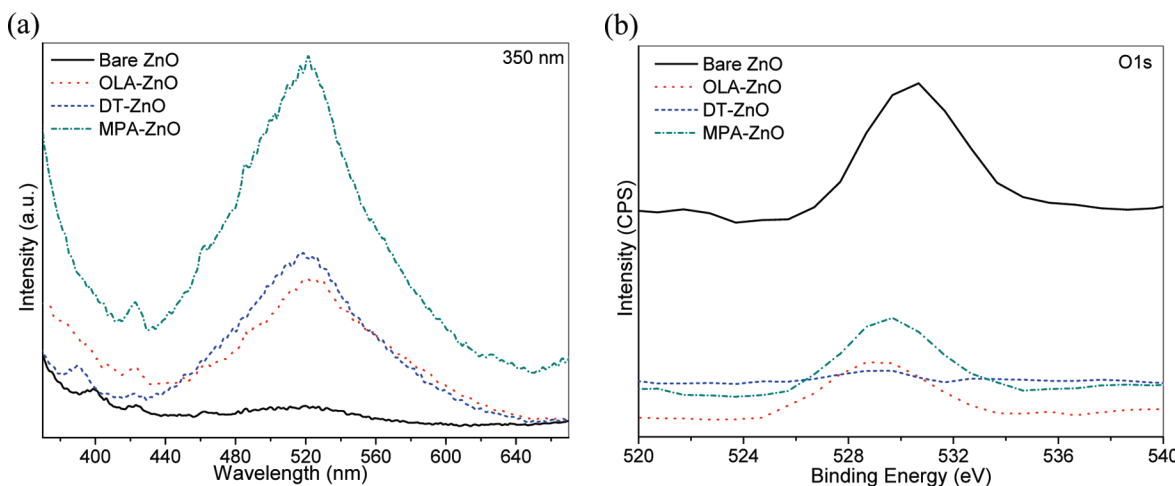


Figure 9. (a) Photoluminescence (PL) emission spectra ($\lambda_{\text{ex}} = 350$ nm) and (b) X-ray photoelectron spectroscopy (XPS) profiles of ZnO NPs functionalized with different ligands.

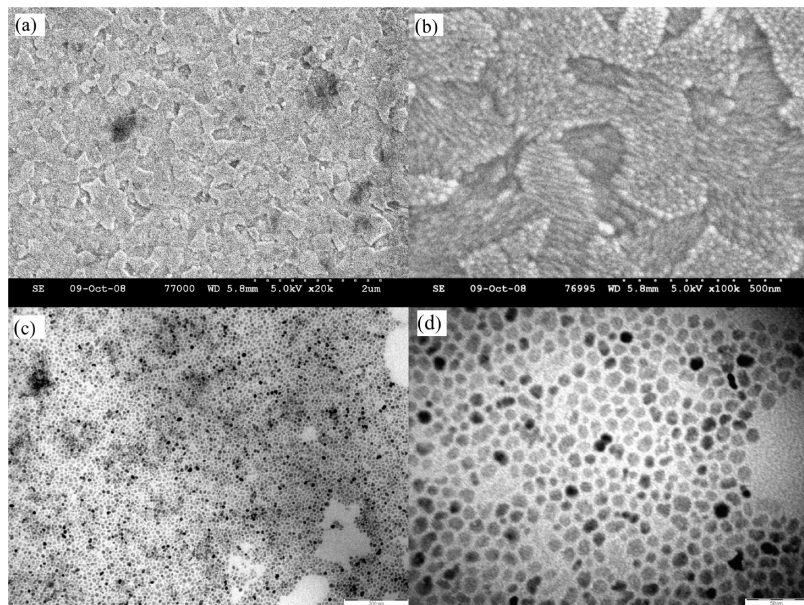


Figure 10. EISA of OLA-ZnO NP superlattices. The (a) low- and (b) high-magnification SEM images of the layered 3D OLA-ZnO NP superlattice film and the (c) low- and (d) high-magnification TEM images of the 2D OLA-ZnO NP superlattice array self-organized on ITO slides.

which can substitute the bound carboxylic groups on the nanoparticle surface to yield the corresponding alkylthiol-functionalized ZnO NPs. Two types of alkylthiol ligands are used here to functionalize the ZnO NPs. One is the alkyl-terminated C_n -SH type ligand with a long hydrophobic (alkyl) tail, for example, 1-dodecanethiol (DT), and another is a carboxylic-acid-terminated COOH- C_n -SH-type ligand with a hydrophilic (carboxylic acid) moiety in the other end, for example, 16-mercaptopentadecanoic acid (MPA). Because of the formation of a more stable ligand-nanoparticle complex by the thiol group rather than carboxylic group, MPA-ZnO NPs have the carboxylic (hydrophilic) exteriors, whereas DT-ZnO NPs have the hydrophobic alkyl exteriors, as shown in Figure 5a. Figure 5c shows that both DT-ZnO and OLA-ZnO NP films having strong CH_2 stretching peaks, implying that the exterior organic shells of the particles are made of a great quantity of alkyl (CH_2) units. The reason that no obvious carboxylic acid absorbance band is detected in MPA-ZnO film is derived from the CH_2 screen effect where the large quantity of CH_2 units dilutes and conceals the small number of carboxylic groups, so only the CH_2 signal can be seen. The freshly prepared

MPA-ZnO NPs (out of ethanol) are soluble in water, whereas the thoroughly dried MPA-ZnO samples are more soluble in ethanol rather than water due to the hydrophobic moieties (CH_2) in MPA molecules much more than the hydrophilic moieties (COOH).

3.3. Self-Assembly of ZnO Nanoparticle Superlattices. The hierarchical self-assembly of the OLA-ZnO particles on ITO-coated glass slides is shown in Figure 10a,b, where the evaporation-induced self-assembly (EISA) patterns from a very diluted NP suspension can be clearly observed. The low-magnification scanning electron microscopy (SEM) image shows the film consisting of many densely packed fractional areas, as shown in Figure 10a. The pattern has a mosaic arrangement and each “tile” can be seen to consist of a multilayer of ordered self-organized superlattice islands under high magnification (Figure 10b). The superlattice island has the feature size of $\sim 10^2$ nm. Figure 10c shows clearly the closely packed, highly ordered and monolayered two-dimensional (2D) NP superlattice array self-organized on the carbon-covered copper grids. The high-magnification view displays the formation of a monolayer of a pseudohexagonal arranged array in Figure 10d.

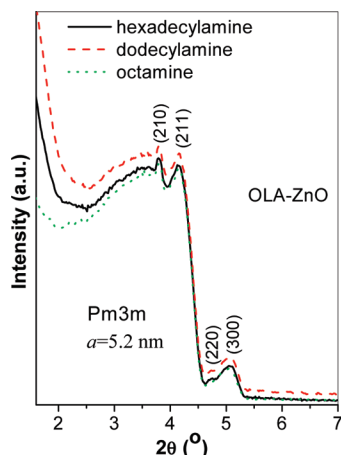


Figure 11. Low-angle XRD pattern of the ordered superlattice arrays formed by PISA of the OLA-ZnO NPs.

The self-assembly tendency of the NPs is witnessed by the images in Figure 10b,c where 3D or 2D patterns formed by EISA can be observed. These results are similar to the previous literature to some extent²¹ but have a larger scale of NP order. The large-scale periodic 2D/3D NP arrays, for the first time, are observed by the well-defined low-angle X-ray diffraction. Figure 11 shows the highly ordered 3D ZnO particle arrays formed by precipitation-induced self-assembly (PISA). Low-angle XRD shows seven well-resolved diffraction peaks in the 2θ range of 2 to 6° that can be indexed as the (210), (211), (220), and (300) reflections of a 3D primitive cubic arrangement. Note that these reflections are superimposed on a large background associated with the regular mesostructure nature described in Figure 10. The samples in Figure 11 are produced by PISA; therefore, it is quite possible to see different sized or shaped aggregates (superlattices). The low-angle diffraction patterns can be considered as the superposition of the diffraction signal caused by numerous different sized subunits, and the diffraction peak, in some directions, are strengthened, while in other directions, are weakened. To some extent, this phenomenon is similar to the low-angle diffraction in cubic mesoporous silica, for example, the SBA-11 system,³⁰ and the real reason is not quite clear for us. The ordered array size estimated by the Scherrer's equation from the width of the reflections is about 45 nm, which is close to the dimensions of the superlattice domains seen in the SEM image in Figure 10b. The diffraction profiles are highly similar for syntheses using the different sized alkylamine spacers, suggesting that this species does not contribute to the particle packing. The intense (210) diffraction peak at 2θ of 3.78° indicates a d spacing of 2.34 nm, corresponding to a large unit cell parameter, $a = 5.22$ nm, which is consistent with the size of the primary OLA-ZnO nanoparticles (ligand shell plus nanoparticle core) seen in Figure 3a–c. The shortening of the C18 chain found in the ordered array may contribute to the compression of the hydrocarbon chain during the formation or the sparse coating. The reason is not quite clear for us. Similar 3D oxide nanoparticle self-assembly has been noted previously by electron microscopy,²¹ but to date, (to the best of our knowledge) no report on XRD patterns typical of highly ordered, cubic-structured nanoparticle arrays has been reported. The XRD evidence strongly suggest that these are some of the most well-ordered superlattices formed by oxide nanoparticles. The PISA leads to 3D self-assembled superlattices, whereas the controlled EISA yields layered 3D NP superlattices on the substrates and monolayer 2D NP superlattices on the grids (carbon films). The superlattice thin films

grown on substrate are almost completely transparent under visible light witnessed by eyes or UV-vis transmission spectrometers.

The transparent superlattice thin films confirm again the formation of well self-organized, less defective, uniform ZnO nanoparticle arrays. We suggest that this process is driven by size/shape regularity of the NPs as well as the repulsive interaction between the hydrophobic alkyl tails on the surfaces of ZnO NPs and the polar solvent molecules, as illustrated in Figure 1. Alkylamines have no influence on the self-assembly of the NPs, as is confirmed by the same result obtained in the absence of alkylamines prior to the assembly. Note that, if nonpolar solvents, such as toluene and hexane, are added to the assembled arrays, they can be redispersed into solution again. Previous work has suggested that such arrays occur via interactions between both ammonium and carboxylate ligands.²¹ However, the absence of amine ligands on the NP surfaces suggests that the assembly is probably via interfacial energy minimization in a multiphase system arising from a balance of hydrophilic and hydrophobic interactions between the particles and the solvent(s).

4. Conclusions

In conclusion, synthesis, functionalization, and self-assembly of the ordered superlattice arrays of ZnO nanoparticles can be obtained in one reaction quickly (in 5 min) with high yield (95%), high efficiency, and low-cost, simple to handle reagents. This methodology has been applied to the synthesis of other metal oxides with success, and the full details have been provided elsewhere.³¹ The functionalization of these particles by long-chain carboxylic acids or alkylthiols improves the dispersivity, size monodispersity, and semiconduction properties (e.g., band gap) dramatically. The 2D or 3D self-assembly process is driven by the interfacial energy minimization between polar solvents and the hydrophobic moieties of OLA-ZnO NPs where well-organized, ordered nanoparticle superlattice structures are produced by either EISA or PISA. We believe this facile method should have promising applications for fabricating other oxide metal superlattices at low temperature and low cost and designing novel oxide nanostructures.

Acknowledgment. This work is supported by the SFI (Science Foundation of Ireland, Grant No. 03/IN3/I1375). We thank Dr. Richard Farrell for his SEM analysis and Dr. Serguei Belochapkin, Materials and Surface Science Institute, University of Limerick, for his XPS analysis.

Supporting Information Available: Particle size distribution (PSD) data. This material is available free of charge via the Internet at <http://pubs.acs.org>.

References and Notes

- (1) Stober, W.; Fink, A.; Bohn, E. *J. Colloid Interface Sci.* **1968**, *26*, 62.
- (2) Mirjafary, Z.; Saeidian, H.; Sadeghi, A.; Moghaddam, F. M. *Catal. Commun.* **2008**, *9*, 299–306.
- (3) Mohanta, K.; Batabyal, S. K.; Pal, A. J. *Chem. Mater.* **2007**, *19*, 3662–3666.
- (4) Rout, C. S.; Raju, A. R.; Govindaraj, A.; Rao, C. N. R. *Solid State Commun.* **2006**, *138*, 136–138.
- (5) Rout, C. S.; Raju, A. R.; Govindaraj, A.; Rao, C. N. R. *J. Nanosci. Nanotechnol.* **2007**, *7*, 1923–1929.
- (6) Suliman, A. E.; Tang, Y. W.; Xu, L. *Sol. Energy Mater. Sol. Cells* **2007**, *91*, 1658–1662.
- (7) Xu, F.; Zhang, P.; Navrotsky, A.; Yuan, Z. Y.; Ren, T. Z.; Halasa, M.; Su, B. L. *Chem. Mater.* **2007**, *19*, 5680–5686.

- (8) Carrey, J.; Carrère, H.; Kahn, M. L.; Chaudret, B.; Marie, X.; Respaud, M. *Semicond. Sci. Technol.* **2008**, *23*, 025003.
- (9) Carrey, J.; Kahn, M. L.; Sanchez, S.; Chaudret, B.; Respaud, M. *Eur. Phys. J.: Appl. Phys.* **2007**, *40*, 71–75.
- (10) Han, D.; Zhang, S. C. *Acta Phys.-Chim. Sin.* **2008**, *24*, 539–542.
- (11) Hlaing Oo, W. M.; McCluskey, M. D.; Huso, J.; Bergman, L. *J. Appl. Phys.* **2007**, *102*, 043529.
- (12) Wang, M.; Na, E. K.; Kim, J. S.; Kim, E. J.; Hahn, S. H.; Park, C.; Koo, K. K. *Mater. Lett.* **2007**, *61*, 4094–4096.
- (13) Yang, M.; Pang, G.; Li, J.; Jiang, L.; Liang, D.; Feng, S. *J. Phys. Chem. C* **2007**, *111*, 17213–17220.
- (14) Meulenkamp, E. A. *J. Phys. Chem. B* **1998**, *102*, 5566–5572.
- (15) Hartlieb, K. J.; Raston, C. L.; Saunders, M. *Chem. Mater.* **2007**, *19*, 5453–5459.
- (16) Li, M. G.; Bala, H.; Lv, X. T.; Ma, X. K.; Sun, F.; Tang, L. Q.; Wang, Z. C. *Mater. Lett.* **2007**, *61*, 690–693.
- (17) Panchakarla, L. S.; Govindaraj, A.; Rao, C. N. R. *J. Cluster Sci.* **2007**, *18*, 660–670.
- (18) Singh, N.; Johri, P.; Soni, D.; Rashmi; Singh, S.; Singh, S. P.; Gupta, P. K.; Sood, K. N.; Chander, H. *Main Group Met. Chem.* **2007**, *30*, 213–221.
- (19) Wang, C.; Li, Q.; Mao, B.; Wang, E.; Tian, C. *Mater. Lett.* **2008**, *62*, 1339–1341.
- (20) Monge, M.; Kahn, M. L.; Maisonnat, A.; Chaudret, B. *Angew. Chem., Int. Ed.* **2003**, *42*, 5321–5324.
- (21) Kahn, M. L.; Monge, M.; Snoeck, E.; Maisonnat, A.; Chaudret, B. *Small* **2005**, *1*, 221–224.
- (22) Viswanatha, R.; Sapra, S.; Satpati, B.; Satyam, P. V.; Dev, B. N.; Sarma, D. D. *J. Mater. Chem.* **2004**, *14*, 661–668.
- (23) van den Brand, J.; Blajiev, O.; Beentjes, P. C. J.; Terryn, H.; de Wit, J. H. W. *Langmuir* **2004**, *20*, 6308–6317.
- (24) Dobson, K. D.; McQuillan, A. *J. Spectrochim. Acta, Part A* **1999**, *55*, 1395–1405.
- (25) Rasmussen, R. S.; Brattain, R. R. *J. Am. Chem. Soc.* **1949**, *71*, 1073–1079.
- (26) Kelly, M. J.; Han, J. H.; Musgrave, C. B.; Parsons, G. N. *Chem. Mater.* **2005**, *17*, 5305–5314.
- (27) Hu, Z. G.; Prunici, P.; Patzner, P.; Hess, P. *J. Phys. Chem. B* **2006**, *110*, 14824–14831.
- (28) Hsieh, P. T.; Chen, Y. C.; Kao, K. S.; Wang, C. M. *Appl. Phys. A* **2008**, *90*, 317–321.
- (29) Wei, X. Q.; Man, B. Y.; Liu, M.; Xue, C. S.; Zhuang, H. Z.; Yang, C. *Physica B* **2007**, *388*, 145–152.
- (30) Zhao, D. Y.; Huo, Q. S.; Feng, J. L.; Chmelka, B. F.; Stucky, G. D. *J. Am. Chem. Soc.* **1998**, *120*, 6024.
- (31) Chen, L.; Xu, J.; Tanner, D. A.; van der Meulen, M.; Phelan, R.; Holmes, J. D.; Morris, M. A. *Chem.—Eur. J.* **2008**, *15*, 440–448.

JP9085766